MAGNETIC FIELD GROWTH AND SATURATION IN PLASMAS WITH LARGE MAGNETIC PRANDTL NUMBER. I. THE TWO-DIMENSIONAL CASE

R. M. KINNEY

Institute of Geophysics and Planetary Physics, UCLA, Los Angeles, CA 90024; kinney@atmos.ucla.edu

B. CHANDRAN

Department of Physics and Astronomy, UCLA, Los Angeles, CA 90024; chandran@physics.ucla.edu

S. COWLEY

Department of Physics and Astronomy, UCLA, Los Angeles, CA 90024; cowley@physics.ucla.edu

AND

J. C. MCWILLIAMS

Department of Atmospheric Sciences, UCLA, Los Angeles, CA 90024; jcm@atmos.ucla.edu

ABSTRACT

In turbulent plasmas, velocities at scales smaller than a scale l_D are strongly damped by viscosity, ν, and magnetic fields below a scale l_R are strongly dissipated by resistivity, η. In galaxies and protogalaxies, $l_D \gg l_R$; i.e., the magnetic Prandtl number, $P_M = \nu/\eta = l_D^2/l_R^2$, is very large. The limit of high magnetic Prandtl number in two dimensions is the focus of this paper. In the kinematic phase of magnetic field growth, when the field is too weak to affect the flow, the field strength grows and the field scale length l_B decreases. Much of the initial growth of the field happens at scales below l_D. In this paper we examine numerically and analytically the growth and saturation of magnetic field on scales less than l_D in two dimensions. If the initial seed field strength is very weak, the field grows and l_B decreases down to the resistive scale l_R before the Lorentz force can affect the magnetic field: once $l_B \sim l_R$ it damps out rapidly. However, if the initial seed field is large enough the field grows until it saturates at a scale l_B with $l_D > l_B > l_R$. In saturation the field strength remains constant and l_B decreases on the resistive time of the saturation scale (i.e., l_B^2/η). The small-scale velocities are insufficient to unwind the small-scale field and produce any kind of inverse cascade. When the scale of the saturation field reaches l_R, the field strength begins to decay. In the initial phase of decay, coherent loops of magnetic field that are formed during saturation persist and act to limit the rate of decay of magnetic energy. Only after these loops have resistively decayed can the final, rapid, kinematic decay take place.

Subject headings: ISM: magnetic fields — magnetic fields — MHD — turbulence

1. INTRODUCTION

The evolution of the magnetic field in a turbulent dynamo depends critically on the magnetic Prandtl number, $P_M = \nu/\eta$, within the turbulent medium, where ν is the kinematic viscosity and η is the resistivity. In astrophysical settings, P_M can be both much less than 1 or much greater than 1. For example, $P_M \sim 10^{-6}$ to 10^{-2} in the solar convection zone (Childress & Gilbert 1995), and $P_M \sim 10^{15}$ in the partially ionized warm gas of the interstellar medium (ISM) in which the viscosity is dominated by the neutral component (Kulsrud & Anderson 1992). The purposes of this paper are to explore both the kinematic stage (in which Lorentz forces can be neglected) and the early nonlinear stages of high-P_M dynamos and to investigate the consequences of the separation of scales that can arise between magnetic and velocity fluctuations when $\eta \ll \nu$.

To treat these stages, it is useful to consider an astrophysically relevant, idealized case. Suppose that a plasma (in, for example, the early galaxy or the protogalaxy) is initially threaded by a weak magnetic field (generated, for example, by a thermoelectric battery during the early stages of structure formation; Kulsrud et al. 1997). Suppose also that at some point in time an external force is turned on that stirs the plasma at some scale l_0 in a statistically steady

way. If the kinetic energy (per unit mass), $E_v \equiv \frac{1}{2}v_0^2$, excited by the stirring is much larger than the magnetic energy, E_B, then magnetic forces can be ignored, and within a few turnover times (l_0/v_0) of the eddies at scale l_0, a Kolmogorov spectrum of hydrodynamic turbulence develops, with a $k^{-5/3}$ inertial range extending from a large scale $\sim l_0$ to a small scale $l_D = \nu^{3/4}\epsilon^{-1/4} \sim R^{-3/4}l_0$, where ϵ is the power input associated with the external force, $R = v_0 l_0/\nu$ is the Reynolds number of the flow, and ν is the viscosity ($v_0 \sim 10^6$ cm s^{-1}, $l_0 \sim 3 \times 10^{20}$ cm, and $l_D \sim 10^{17}$ cm for warm partially ionized interstellar plasma; Kulsrud & Anderson 1992). Because the eddy turnover time scales as $l^{2/3}$ within the inertial range, the smallest eddies turn over most rapidly and tangle the magnetic field lines most effectively. While the dynamo is in the kinematic stage, the magnetic energy exponentiates roughly once per turnover time of the eddies at scale l_D, and the dominant length scale l_B of the magnetic field decreases exponentially at roughly the same rate (Batchelor 1950; Kazantsev 1968; Kraichnan 1976; Kulsrud & Anderson 1992; Gruzinov, Cowley, & Sudan 1996). This small eddy turnover time, $\tau_d \sim R^{-1/2}l_0/v_0$, is $\sim 10^5$ yr within the partially ionized warm gas of the ISM (Kulsrud & Anderson 1992). Because τ_d is comparatively short, there can be many exponentiations of the magnetic energy within a single large eddy turnover time

when R is large (10^2 times in the warm ISM). We assume that the eddy turnover is initially unimpeded by magnetic forces; i.e., the initial weak field B_I has less energy than the eddies at scale l_D. This gives $B_I < 0.2$ μG for the warm ISM. Thus, in the early stage of the high-P_M dynamo, the field is expected to be highly tangled.

The magnetic field observed in the high-P_M interstellar medium is not, however, highly tangled. Observations indicate that the component of the galactic magnetic field that is coherent over kiloparsec scales, B_u, is ~ 2–4 μG and that the total magnetic energy is between 2 and 10 times as large as the energy associated with B_u (Zweibel & Heiles 1997). Thus, a considerable fraction of the galaxy's magnetic energy is concentrated on length scales comparable to or greater than the dominant length scales of interstellar turbulence (Larson 1979; Spangler & Cordes 1998). If the observed galactic field is generated by a turbulent dynamo in the warm ISM, it cannot be due to linear kinematic effects alone. In other words, the observed large-scale field in the galaxy is an intrinsically nonlinear phenomenon, and the nonlinear evolution of $\boldsymbol{B}$, starting from when l_B is still $\ll l_D$, is critical. Clearly, if a dynamo in the warm interstellar medium is to work, l_B must evolve nonlinearly from $l_B \ll l_D$ through $l_D \ll l_B \ll l_0$ to $l_B \gg l_0$. How such a multistage inverse cascade is possible is not yet clear.

Recognizing the problem of small-scale fields, Parker (1979) argued that before they can significantly affect the velocity turbulence, small-scale magnetic fields are removed either by fast magnetic reconnection or by buoyancy. However, magnetic reconnection does not appear to suppress the small-scale field in numerical solutions of homogeneous turbulence. Several numerical solutions (Meneguzzi, Frisch, & Pouquet 1981; Cattaneo & Hughes 1996) and closure calculations (Pouquet, Frisch, & Léorat 1976; Chandran 1997) have shown that with $l_D \lesssim l_B$ and $P_M \sim 1$ the initial magnetic field grows on scales $l_B \sim l_D \sim l_R$, then as nonlinearity becomes important l_B grows. It is expected that the velocity spectrum during this inverse cascade is Kolmogorov-like for length scales $l > l_B$. For $l < l_B$, there is local equipartition between velocity and magnetic field in k-space [$\rho v^2(k) \sim B^2(k)$], where the classical presumption is that motions on these scales are Alfvén waves (Kraichnan 1965). Thus, there is evidence for an inverse cascade of magnetic energy when $l_D \ll l_B \ll l_0$ due to nonlinear interactions. There is also evidence for an inverse cascade to scales $l \gg l_0$ (Meneguzzi et al. 1981; Balsara & Pouquet 1999). An inverse cascade without resistance playing a role must somehow involve unwinding small-scale fields to arrest their amplification while amplifying large-scale fields. Mean field dynamo theory has been used extensively to describe magnetic fields in galaxies (Ruzmaikin, Shukurov, & Sokoloff 1988). This is, in its usual exposition, a linear theory that essentially ignores the growth of small-scale field. It is therefore not clear that such a theory should describe galactic fields, although several authors have suggested reasons why it might (Field, Blackman, & Chou 1999; Brandenburg & Donner 1997).

The focus of this paper is on the early stages of the non-linear evolution toward a large-scale magnetic field. Because $l_B \ll l_D$ at the onset of the nonlinear stage, the magnetic field behaves like a tangled mass of rubber bands, making the turbulent medium elastic and converting the turbulence from hydrodynamic motions into overdamped oscillatory magnetoelastic waves, which saturates the

growth of E_B. The details of this process in the high-P_M regime, however, remain poorly understood and have not been treated through direct numerical simulation. While our goal is to provide analysis and simulations of this non-linear stage in a physical, three-dimensional dynamo, we here restrict ourselves to the antecedent and more modest goal of describing the field evolution in two-dimensional high-P_M turbulence. Although Zeldovich (1957) and Cowling (1957) have proven that the magnetic energy must ultimately decay to 0 in a two-dimensional flow, our exploration of the high-P_M, two-dimensional pseudodynamo will, we believe, provide physical insight that will prove valuable in future treatments of the three-dimensional case.

Since the evolution of the magnetic field on scales smaller than l_D is driven primarily by the velocities at scale $\sim l_D$, we can describe the key physics of early-stage dynamos by simulating only scales $\lesssim l_D$. The plasma in our simulations is stirred by a random external force that simulates the nonlinear hydrodynamic energy transfer from the inertial range ($l_0 > l > l_D$) to the dissipation range ($l < l_D$). In the absence of magnetic fields, this force leads to the type of power spectra found in numerical simulations of the dissipation range in hydrodynamic turbulence (Chen et al. 1993). Our small-domain simulations can be interpreted as simulating small regions within a high–Reynolds number flow such that a Reynolds number based upon our domain size is small. If l_B grows during the nonlinear stage and becomes comparable to l_D, then our calculations can no longer be meaningfully continued, but such growth in l_B is not found in our two-dimensional simulations, meaning the inverse cascade we seek is absent. On a longer timescale, eddies with $l > l_D$ will continue to tangle the field, since these slower eddies still have larger kinetic energy than those at $l = l_D$. This part of the evolution is not examined here, although we expect no change in the conclusion that there is no inverse cascade. A future paper will examine the three-dimensional case.

A point that will not receive much attention in this paper is related to the anisotropy of the plasma viscosity tensor (i.e., the inequality $v_\parallel \gg v_\perp$, where $v_\parallel$ and $v_\perp$ are parallel and perpendicular viscosities; Braginskii 1965). This anisotropy is important in a fully ionized plasma but not in the partially ionized warm gas of the ISM, where neutrals dominate the viscosity. However, when there is a uniform background magnetic field, then slow waves (which change the strength of the local magnetic field) are much more strongly damped than shear Alfvén waves (Goldreich & Sridhar 1995; Quataert 1998). This linear damping produces anisotropy in the magnetic spectrum (Oughton 1996), but the influence of the background field on the nonlinear interaction of Alfvén waves also strongly affects the anisotropy of the turbulent magnetic spectrum (Kinney & McWilliams 1995). Nevertheless, the behavior of plasmas with large P_M and anisotropic viscosity, while deserving of more study, remains beyond the scope of the present paper.

This paper describes analytical results for the high-P_M equations and results from direct numerical solutions using a semi-Lagrangian algorithm described in the Appendix. In § 2, we give an overview of the different stages of the two-dimensional pseudodynamo. We consider the kinematic stage in more detail in § 3. In § 4 we present numerical and semianalytic results describing the first nonlinear stage in which the magnetic energy is saturated but has not yet begun to decay resistively. The nonlinear and kinematic

decay stages are described in § 5. We discuss the implications of our work and its relation to some previous studies in § 6.

2. MAGNETIC ENERGY GROWTH, SATURATION, AND SCALE EVOLUTION: THE TYPICAL SCENARIOS

We calculate numerical solutions of MHD in a highly viscous but weakly resistive regime. The magnetic field is divergenceless, $\nabla \cdot \boldsymbol{B} = 0$, and is given in terms of a scalar potential, so that $\boldsymbol{B} = \hat{\boldsymbol{z}} \times \nabla A$, where A obeys

$$\partial_t A + \boldsymbol{v} \cdot \nabla A = \eta \nabla^2 A . \tag{1}$$

Some of our calculations use a hyperresistive term $-\eta_4 \nabla^4 A$, which allows an extended dynamical range of scales. The effect of using hyperresistivity is discussed in the Appendix. Our computational domain is chosen such that the largest available scale is the viscous scale and the smallest available scale is the resistive scale. The velocity evolution is driven by a large-scale random forcing, and the viscous force dominates the inertial force (see Appendix for details), so that $\boldsymbol{v}$ obeys

$$\rho v \nabla^2 \boldsymbol{v} = -(\nabla \times \boldsymbol{B}) \times \boldsymbol{B} + \nabla p - \boldsymbol{F} ,$$

$$\nabla \cdot \boldsymbol{v} = 0 , \tag{2}$$

with $\boldsymbol{F}$ a large-scale random function with a prescribed correlation time and the plasma density, ρ, is assumed constant. The magnetic field is initialized with a random spectrum peaked at the largest scales. The dimensionless variables are such that the length of the domain is 1, and $\rho = 1$. We choose $\boldsymbol{F}$ so that the kinetic energy is 1 when $\boldsymbol{B} = 0$, and $t = 1$ is a single large eddy turnover time.

In this paper, we discuss two magnetic field evolution scenarios. The linear or kinematic scenario occurs when the initial field strength, B_I, is extremely weak ($B_I^2 \ll \rho v_D^2 l_R^2/l_D^2$). The nonlinear scenario occurs when the initial magnetic field is above a certain threshold ($B_I^2 \gtrsim \rho v_D^2 l_R^2/l_D^2$), although still such that $B_I^2 \ll \rho v_D^2$. A third possible scenario, with $B_0^2 \gg \rho v_D^2$, is not applicable to the astrophysical problem and is not discussed here.

In the linear or kinematic scenario, the initially weak magnetic field grows in strength exponentially in time while l_B decreases exponentially in time. The kinematic growth phase is terminated when the scale of the magnetic field reaches the resistive scale (i.e., $l_B \sim l_R$). Following the growth phase is a decay phase in which the field strength decays exponentially in time, while l_B remains $\sim l_R$. The initial field strength in the kinematic scenario is sufficiently small that the magnetic field is unimportant dynamically at all times during its evolution.

In the nonlinear scenario, on the other hand, the magnetic field does become dynamically important. Figure 1 shows the time history of magnetic energy, $E_B = \frac{1}{2} \int B^2 \, dx$, and kinetic energy $E_v = \frac{1}{2} \rho \int v^2 \, dx$, in a typical nonlinear scenario calculated on a 1024^2 grid. The energy in the forcing $\boldsymbol{F}$ is 1, and the correlation time of $\boldsymbol{F}$ is $\tau = 1$. The initial magnetic energy is 0.1, and $R_M = l_0/l_R \approx 1000$. The evolution can be divided into four stages: kinematic growth ($t < 2$), nonlinear saturation ($2 < t < 10$), nonlinear decay ($10 < t < 52$), and kinematic decay ($t > 52$). The boundaries between these phases are marked with dotted lines in the
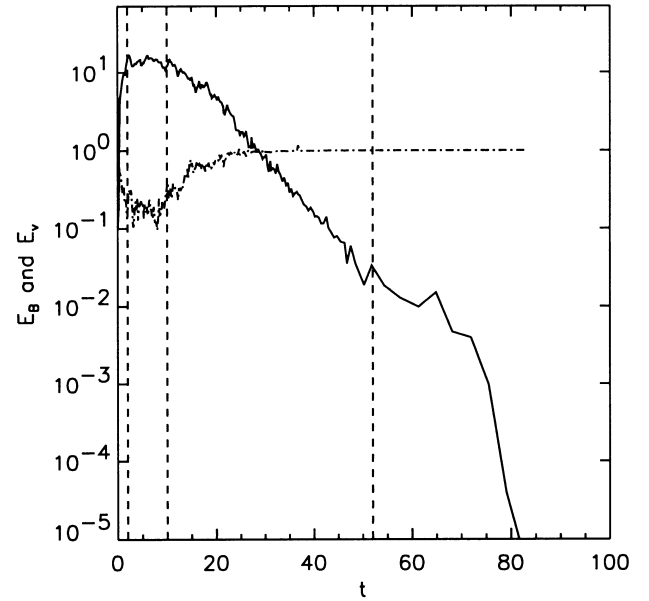
figure. Figure 2 shows the time evolution of the mean wavenumber

FIG. 1.—Magnetic (*solid line*) and kinetic (*dot-dashed line*) energy vs. time for typical nonlinear solution [$E_B(0) = 0.1$, $\tau = 1$] showing kinematic growth, saturation, nonlinear decay, and kinematic decay phases. Time is measured in units of the eddy turnover time.

$$\bar{k}^2 = \frac{\int B^2}{\int A^2} \tag{3}$$

for the same solution.

During the first phase, kinematic growth, the magnetic field stretches and folds due to the stirring motion of the
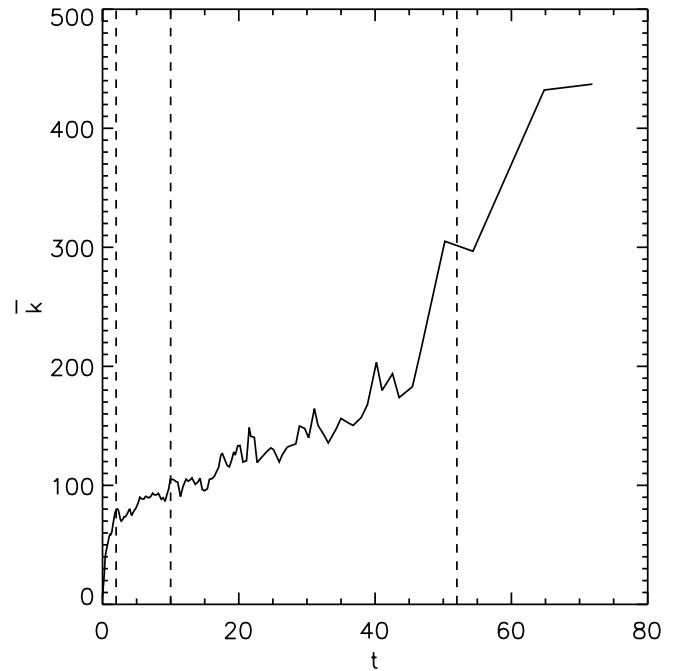

FIG. 2.—Mean wavenumber vs. time for the same solution as in Fig. 1. The mean wavenumber grows rapidly during the kinematic growth phase, grows slowly during the saturation and nonlinear decay phases, and stays peaked during the kinematic decay phase.

fluid. In two dimensions, the magnetic field strength can grow only by a folding of magnetic field lines (i.e., $Bl_B \sim$ constant). Thus, an exponential growth of the magnetic field strength implies exponential growth of the mean wavenumber. The nonlinear saturation phase begins when the magnetic field lines become stretched to the point that they resist further folding because the elastic tension in the field lines acts in opposition to the driving flow. This gives $B^2 = B_{\mathrm{sat}}^2 \sim \rho v_D^2$ (see below) and $l_B \sim l_D(B_I/B_{\mathrm{sat}})$ at the beginning of saturation. During this phase, resistive effects weaken the stretched magnetic field, but the fluid flow quickly stretches it back to its saturated strength while moving it to smaller scales. Thus, the magnetic energy stays roughly constant during this phase, while the mean wavenumber increases slowly. At the same time, tension in the magnetic field opposes the motion of the fluid, decreasing the total kinetic energy from what it would be in the absence of a magnetic field. The duration of the saturated phase increases with R_M and can last arbitrarily long, but in two dimensions at finite R_M the magnetic energy must always eventually decay to 0 (Zeldovich 1957). This decay occurs in two distinct phases. During the nonlinear decay phase, the magnetic energy decays exponentially, but the rate is slowed by the magnetic forces. The magnetic flux becomes tied up in magnetic loop structures, which (because of tension in the magnetic field lines) resist straining by the fluid flow. The mean wavenumber continues to increase as these structures shrink in size. In the final stage of kinematic decay, structures are absent and the mean wavenumber reaches and remains at the resistive wavenumber while the total magnetic energy decays rapidly to 0. We explore each of these phases in detail below.

3. KINEMATIC PHASE

The kinematic growth of magnetic fields (i.e., the magnetic field evolution when the field is too weak to affect the fluid flow) is the most widely studied and well-understood magnetic dynamo process (Childress & Gilbert 1995; Moffatt 1978). When the resistance is ignored, the magnetic field obeys the well-known frozen-in condition. The amplification of the magnetic field by the flow can be understood in terms of the stretching of magnetic field lines. In an incompressible flow, the lengthening of a flux tube (a tube containing a field line) is accompanied by a narrowing of the tube. Then flux conservation requires an increase in B.

To illustrate the stretching of a magnetic field line by random flows, consider the simple model problem of a line element with length $L(t)$ stretched by steady plane-parallel flows. After each correlation time τ_L, let the flow direction be randomized. Consider the stretching during one correlation time by the flow $v = v'y\hat{x}$ (where the velocity gradient v' has units of inverse time). Simple geometry gives

$$L^2(t + \tau_L) = L^2(t)(1 + 2v'\tau_L \sin \theta \cos \theta + v'^2 \tau_L^2 \sin^2 \theta) , \quad (4)$$

where $\hat{x} \cdot L(t) = L(t) \cos \theta$. The angle θ will be randomly distributed. Thus, the average change in the square of the length of the field line is

$$\langle \Delta L^2(t) \rangle = L^2(t + \tau_L) - L^2(t) = \tfrac{1}{2} L^2(t) v'^2 \tau_L^2 . \quad (5)$$

For small τ_L, one can write a differential equation,

$$\frac{dL^2}{dt} = \frac{1}{2} L^2 v'^2 \tau_L . \quad (6)$$

Since by flux conservation $B \propto L$, we get

$$B^2 \sim B_0^2 e^{\gamma_B t} , \quad (7)$$

with $\gamma_B \approx \tfrac{1}{2} v'^2 \tau_L$. The amplification can be further visualized by imagining a square entrained in the flow being stretched and sheared into a very distorted parallelogram and identifying τ_L as the Lagrangian correlation time traveling with the square. Clearly, the shear matrix ∇v seen in the moving frame determines the growth of B^2 (Gruzinov et al. 1996). Since $\nabla \cdot v = 0$, stretching of field lines requires that the variations of B perpendicular to B itself become shorter in scale. In fact, one expects $Bl_B =$ constant. Thus, during field exponentiation, $l_B \sim \bar{k}^{-1}$ decreases exponentially at a rate $\tfrac{1}{2}\gamma_B$.

In the short correlation-time limit, $\tau_L v' \ll 1$ (often called the limit of small Kubo number), the evolution of the magnetic field during kinematic growth can be calculated in some detail. We define the vector potential power spectrum

$$M_{k_x k_y} = \langle A_{k_x k_y} A_{k_x k_y}^* \rangle , \quad (8)$$

where the angle brackets indicate an average over an ensemble of realizations of the turbulent velocities. Assuming that the velocities are incompressible and statistically isotropic, we can write

$$\langle v_{k_x k_y}(t_1) v_{k_{x'} k_{y'}}(t_2) \rangle = J(k)\theta_k(t_1, t_2)(I - \hat{k}\hat{k})$$
$$\times \delta_{k_x, -k_{x'}} \delta_{k_y, -k_{y'}} , \quad (9)$$

where $\hat{k}$ is a unit vector pointing in the direction of k, I is the unit tensor, and $J(k)$ is the azimuthally averaged velocity power spectrum. The correlation function $\theta_k(t_1, t_2)$, assumed for simplicity to be independent of k, is 1 for $t_1 = t_2$, and decays to 0 for large $|t_2 - t_1|/\tau$, so that

$$\lim_{(t/\tau) \to \infty} \int_0^t dt_1 \int_0^t \theta(t_1, t_2) = \tau t , \quad (10)$$

which defines the correlation time τ.

When the scale length of the magnetic field is much smaller than the velocity scale length, but still large enough that resistivity can be neglected, the time derivative of equation (8), using equations (1) and (9), leads to

$$\frac{\partial M}{\partial t} = \gamma \frac{\partial^2 M}{\partial r^2} , \quad (11)$$

where

$$r \equiv \ln k + 2\gamma t , \quad (12)$$

$$\gamma = \frac{\tau}{16} \left\langle \int dx\, dy\, |\nabla \times v|^2 \right\rangle . \quad (13)$$

This two-dimensional result was derived in a different form by Kulsrud & Anderson (1992) and Gruzinov et al. (1996), and an analogous equation for three-dimensional turbulence was derived by Kazantsev (1968). From equation (13), we may easily derive the evolution of the magnetic spectrum when the initial spectrum is highly peaked at $k = k_0 \gg k_D$,

$$\langle B(k) \cdot B^*(k) \rangle = \frac{B_0^2}{2\pi k_0^2 \sqrt{4\pi\gamma t}} \exp \left\{ \frac{-[\ln(k/k_0) - 2\gamma t]^2}{4\gamma t} \right\} . \quad (14)$$

Clearly, the peak of the magnetic field spectrum moves to smaller scales and the volume of k-space occupied by the magnetic field increases. Integrating equation (14) over

k-space, we get exponential growth of B^2 with rate 8γ (thus, $\gamma_B = 8\gamma$). We note that at a fixed $k > k_0$, $\langle |B(k)|^2 \rangle$ will initially grow and ultimately decay; however, the peak in k-space of $k^2 \langle |B(k)|^2 \rangle$ (the energy density per unit log k) does grow. In Figure 3, we plot the kinematic growth rate, γ_B, measured in numerical solutions versus τ, where τ is the Eulerian correlation time of F and therefore the flow. For $\tau < 0.1$, the agreement with the value calculated from equation (13) is good, but our calculation fails at larger values of τ. The τ plotted in Figure 3 is the Eulerian correlation time of the velocity; however, for the growth one must use the Lagrangian correlation time τ_L (the correlation time measured in a frame moving with the fluid) which becomes a constant independent of τ for large $\tau \sim \mathcal{O}(1)$. This effect explains the saturation of γ_B with increasing τ in Figure 3. In reality, $\tau v' \sim 1$ for turbulent velocities at the scale l_D in a Kolmogorov cascade; however, it is useful here to have τ as an independent parameter to aid our understanding.

When the initial B field is very small ($B_0^2 < \rho v_D^2 \, l_R^2/l_D^2$), the field evolves as in the linear or kinematic scenario (see § 2), where the typical wavenumber, k_B, increases exponentially in time until resistivity cannot be neglected (i.e., when $k_B \sim l_R^{-1}$). This happens in a few turnover times and accounts for the rapid initial jump in $\bar{k}$ in Figure 2. The approximate resistive evolution of the magnetic energy can be obtained by assuming that M satisfies equation (11) for $k < l_R^{-1}$ and drops abruptly to 0 for wavenumbers larger than l_R^{-1}. In this approximation, if the magnetic energy is initially E_{m0} and M is initially peaked sharply about the wavenumber k_0, then

$$E_B = \frac{E_{m0}}{2} \left\{ 1 + \mathrm{erf}\left[\frac{\ln(k_R/k_0) - 6\gamma t}{\sqrt{4\gamma t}} \right] \right\} e^{8\gamma t} . \quad (15)$$

Equation (15) gives the transition from a nonresistive kinematic energy growth rate of 8γ to resistive decay of the energy at large times at the rate $e^{-\gamma t}$. The transition between growth and decay occurs after a time of order $\gamma^{-1} \ln(k_R/k_0)$.
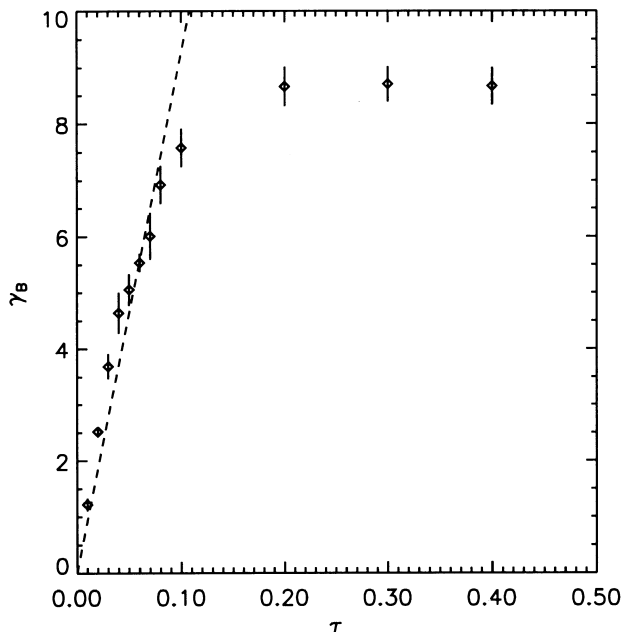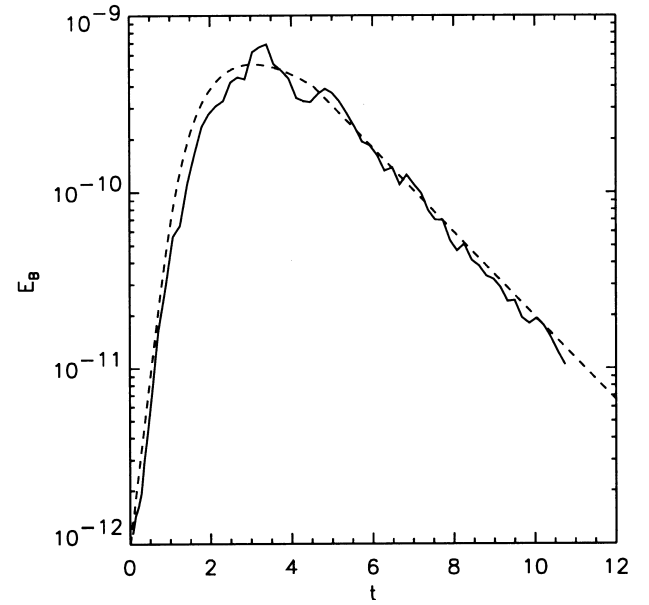

FIG. 4.—Magnetic energy vs. time for kinematic evolution at $\tau = 0.025$. The dashed line is a one-parameter fit to the closure theory prediction.

Figure 4 shows the time history of magnetic field energy for a case with very weak magnetic field and $\tau = 0.025$. The dashed line is one-parameter fit (varying k_R) to equation (15). The value of γ, calculated from equation (13) using the solution data for v, gives the initial growth rate and final decay rate quite accurately, and the value for k_R obtained from the fit is consistent with the scaling estimate $k_R^2 \sim v/(l_D \eta)$.

An important feature of the magnetic field during kinematic growth is its folded structure. The magnetic field folds reverse rapidly across the field on the scale l_B. The variation along the folds is on the scale of the variation of the velocity l_D, which is of order the domain size in our solutions. In Figure 5 we compare gradients along and across B,
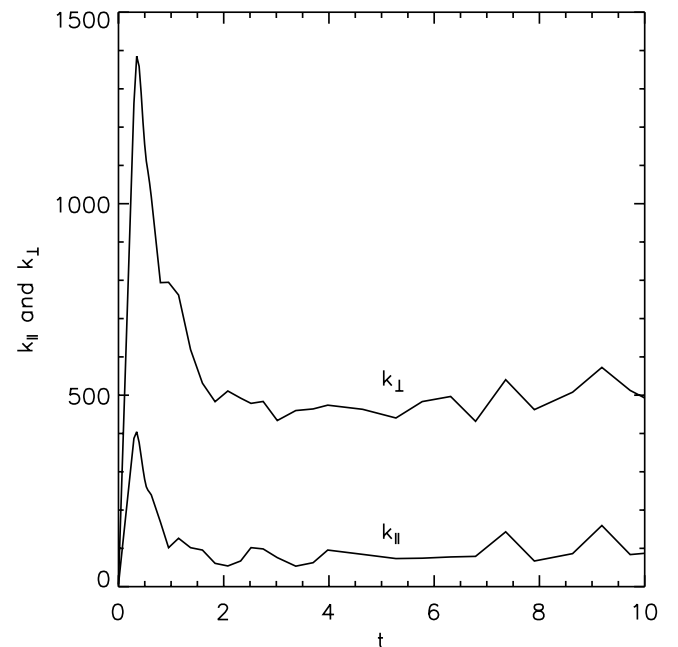

FIG. 3.—Kinematic growth rate γ_B of magnetic energy vs. velocity correlation time τ, shown along with the theoretical small-τ prediction. The growth rate is linear for small τ but becomes constant for larger τ.

FIG. 5.—Magnetic field gradient wavenumbers along ($k_\parallel$) and across ($k_\perp$) the local magnetic field direction for $E_B(0) = 0.1$, $\tau = 1$.

defined as

$$k_\parallel^2 = \frac{\int |B \cdot \nabla B|^2}{(\int B^2)^2} ,$$

$$k_\perp^2 = \frac{\int |(\hat{z} \times B) \cdot \nabla B|^2}{(\int B^2)^2} , \qquad (16)$$

where the integrals are over the volume of the simulated domain. The perpendicular gradient, $k_\perp$, grows to many times larger than the parallel gradient, $k_\parallel$. This result can be understood from Lagrangian analysis. Let $r(r_0, t)$ be the position of a fluid element that was at r_0 at time $t = 0$. The magnetic field at time t at r is given by

$$B(r, t) = B_0 \cdot \nabla r , \qquad (17)$$

a result sometimes referred to as Lundquist's identity. Using flux conservation, $B \sim B_0 \, l_D/l_B$, we have

$$B \cdot \nabla B = B_0 \cdot \nabla_0(B_0 \cdot \nabla_0 r) \sim \frac{B_0^2 \, l_D}{l_B^2} \sim \frac{B^2}{l_D} , \qquad (18)$$

$$\nabla B^2 \sim \frac{B^2}{l_B} . \qquad (19)$$

The dominance of $k_\perp$ over $k_\parallel$ implies highly folded fields with only moderate bending of the folds. Typical folded structures can be seen in the current $j = \hat{z} \cdot (\nabla \times B)$ in Figures 6 and 7. The structure also depends on the correlation time τ. For long correlation times (steady flows), the field is concentrated in the regions of high velocity shear as in Figure 6. For shorter correlation times, the folds are
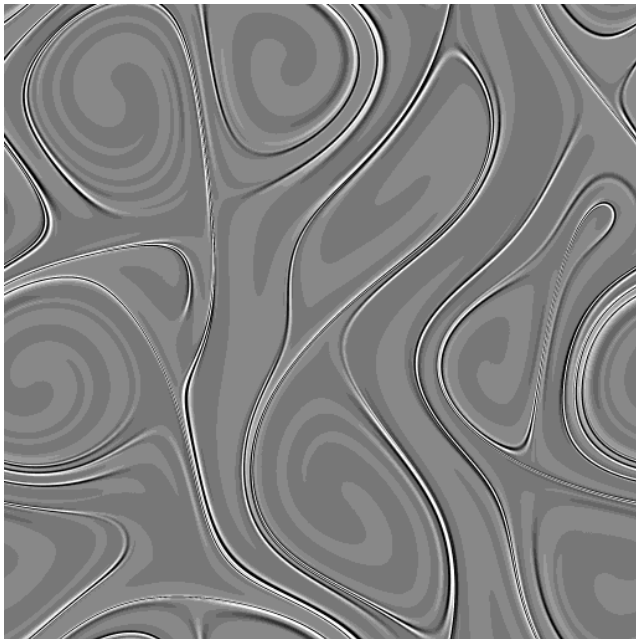

FIG. 7.—Current of a kinematic solution with correlation time $\tau = 0.025$ (2048^2 grid, $R_M \sim 2000$). The current sheets are folded to produce a much more space-filling field, although most of the energy is still at the scale of the sheet thickness.

more space filling as in Figure 7. This difference in structure is not discernible from the magnetic spectra. As we show below, the folded nature of the B structure is important in understanding the nonlinear saturation.

4. NONLINEAR SATURATION

In this section we examine the saturation of the magnetic field strength when it becomes strong enough to alter the flow. A simple calculation shows that when a straight field is bent by a small perturbation, the perturbation shrinks exponentially with a rate $B^2/\nu\rho$. This is the damping rate of an Alfvén wave in the highly viscous regime. The saturated state is thus a competition between the driving flow which is attempting to bend field lines and the viscous relaxation attempting to straighten them.

To understand the saturation process, we introduce an idealized model which contains the key features of the saturation dynamics. We consider a strong "striped" field $B_0(y)\hat{x}$, where B_0 varies on a small scale l_B ($l_B \ll l_D$). The forcing at scales l_D will cause this field to be distorted. However, as long as B_0 is sufficiently large, such distortions are small. Let $\boldsymbol{\xi}(r_0, t)$ be the displacement of the plasma from the original position r_0 so that $v = \partial_t \boldsymbol{\xi}$. In this Lagrangian description we have $B = B_0 \cdot \nabla_0 r$ and $B \cdot \nabla B = B_0 \cdot \nabla_0(B_0 \cdot \nabla_0 r) = B_0^2(y)\partial^2\boldsymbol{\xi}/\partial x_0^2$. Taking the curl of equation (2) and treating $\nabla_0 \boldsymbol{\xi}$ as small, we obtain

$$\rho_0 \nu \nabla_0^2 \left(\hat{z} \cdot \nabla_0 \times \frac{\partial \boldsymbol{\xi}}{\partial t} \right) + \hat{z} \cdot \nabla_0$$

$$\times \left[B^2(y) \frac{\partial^2 \boldsymbol{\xi}}{\partial x_0^2} \right] = \hat{z} \cdot \nabla_0 \times F(r_0, t) . \qquad (20)$$

We separate the large-scale (at $\sim l_D$) displacement, $\bar{\boldsymbol{\xi}}$, and small-scale (at $\sim l_B$) displacement $\tilde{\boldsymbol{\xi}}$. Note $\nabla_0 \xi$ is small when

FIG. 6.—Current ($\hat{z} \cdot \nabla \times B$) of a kinematic solution (2048^2 grid, $R_M \sim 2000$) in a stationary velocity field ($\tau = \infty$) at the time of maximum magnetic energy. White indicates field coming out of the page, and black indicates current into the page. The field is concentrated into a few thin sheets where the shear is strongest.
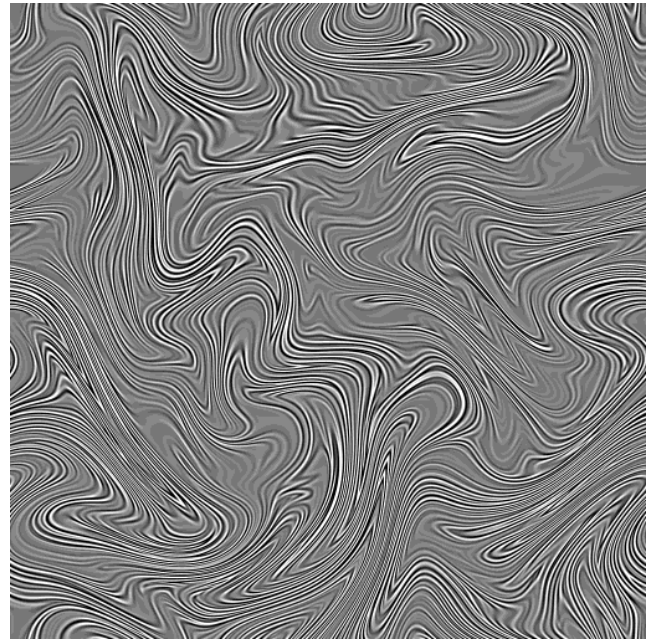
$\bar{\xi} \ll l_D$ and $\tilde{\xi} \ll l_B$. We take the small-scale average of B_0^2, $\bar{B}_0^2$, to be constant on the large scale. Averaging equation (20) we obtain an equation for $\bar{\xi}$. We solve for the Fourier transform of $\bar{\xi}(r, t)$, $\bar{\xi}_k(t)$, to obtain

$$\bar{\xi}_k(t) = \int_0^t dt' e^{-\gamma_k(t-t')} v_{0k}(t) , \qquad (21)$$

where $v_{0k}(t) = (\boldsymbol{I} - \hat{k}\hat{k}) \cdot \boldsymbol{F}_k(t)/\nu\rho_0 k^2$ is the velocity in the kinematic limit and

$$\gamma_k = \frac{\bar{B}_0^2}{\nu\rho_0} \frac{k_x^2}{k^2} . \qquad (22)$$

As expected, motions that do not bend the field lines are unopposed. For nonzero k_x and a steady v_0 independent of t, ξ simply approaches an asymptotic value exponentially.

If v_0 varies in time with the same statistics as in the kinematic case, (see eq. [9]), then again by assuming that τ is very short ($\gamma_k \tau, v_0' \tau \ll 1$), we can compute the evolution of the mean square displacements

$$\langle \bar{\xi}(r_0, t)\bar{\xi}(r_0, t) \rangle = \tau \sum_{k, k_x \neq 0} \frac{1 - e^{-\gamma_k t}}{\gamma_k}$$
$$\times J(k)(\boldsymbol{I} - \hat{k}\hat{k}) + \tau t \sum_{k, k_x = 0} J(k)\hat{x}\hat{x} . \quad (23)$$

We note that for small times ($\gamma_k t < 1$) all terms behave diffusively ($\xi^2 \propto t$). However, for large times ($\gamma_k t > 1$) only the displacement along the field line is diffusive while displacements across the field lines are bounded.

To obtain a general expression for the saturation, we first replace $\gamma_k t$ with $\frac{1}{2}\int_0^t dt \langle B^2 \rangle/\nu\rho_0$. The growth rate of $\langle B^2 \rangle$ is proportional to $\partial_t \langle |\boldsymbol{V}_0 \times \boldsymbol{\xi}|^2 \rangle$. Let γ_B be the growth rate from diffusive growth of ξ in the kinematic case ($\gamma_B = 8\gamma$ from eq. [15]). Then the time derivative of equation (23) indicates a growth rate of $\gamma_B \exp\left(-\int_0^t dt \frac{1}{2}\langle B^2 \rangle/\nu\rho_0\right)$. This leads to

$$\frac{d\langle B^2 \rangle}{dt} = \langle B^2 \rangle\gamma_B \exp\left(-\int_0^t dt \frac{1}{2}\frac{\langle B^2 \rangle}{\nu\rho_0}\right), \qquad (24)$$

which has the solution

$$\langle B^2 \rangle = \frac{B_{sat}^2 B_I^2 e^{\gamma_B t}}{B_{sat}^2 + B_I^2 e^{\gamma_B t}}, \qquad (25)$$

where B_I^2 is the initial field and

$$B_{sat}^2 = 2\nu\rho_0 \gamma_B \sim \rho_0 v_D^2 . \qquad (26)$$

The latter estimate comes from setting $\gamma_B \sim v_D/l_D$ and recognizing that at the viscous scale $v_D \sim \nu/l_D$. While the derivation of equation (25) is not rigorous, it expresses the essential dynamics of saturation: the magnetic field grows until the viscous relaxation rate, $\frac{1}{2}B^2/\nu\rho_0$, equals the kinematic growth rate, γ_B.

Figure 8 shows the magnetic and kinetic energy versus time for numerical solutions in which the magnetic energy grows to be dynamically important with $\tau = 1$. The solutions are initialized with different magnetic energy but, in agreement with the analysis, they all saturate at the same field strength. Because the field can only grow by becoming more tangled, folding during the kinematic phase conserves flux so that $Bl_B \approx B_I l_D$. Thus, l_B in saturation is proportional to B_I.

The total kinetic energy in these solutions is less than the energy that would be obtained for the same external force $\boldsymbol{F}$
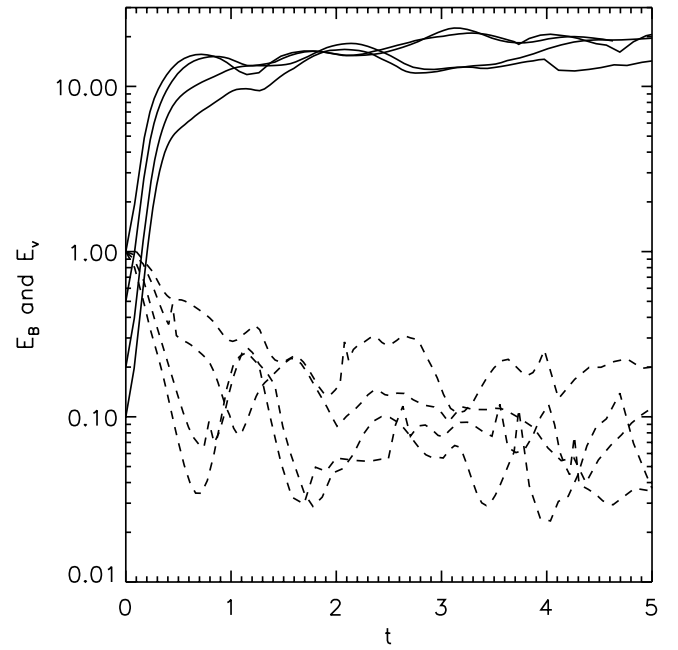

FIG. 8.—Total magnetic (*solid lines*) and kinetic (*dashed lines*) energy of solutions with nonlinear magnetic force included and $\tau = 1$. Solutions with initial energy $E_B(0) = 0.1$, 0.2, 0.5, and 1 all saturate at $E_B \approx 10$–15. Although the energy in the external forcing is 1, the total kinetic energy is reduced to $E_v \approx 0.1$ because the tension in the magnetic field lines directly opposes the driving.

in the absence of magnetic forces. This is because the Lorentz force has a large-scale component that acts in direct opposition to the forcing and coherently reduces the amplitude of the velocity. In the solutions shown in Figure 8, with $\tau = 1$, the kinetic energy is $\approx 10\%$ of the kinetic energy that would result in the absence of magnetic forces. For smaller τ, the velocity changes faster than the magnetic field can adjust to cancel it, so reduction of kinetic energy is correspondingly less. In Figure 9 we plot the saturated mag-
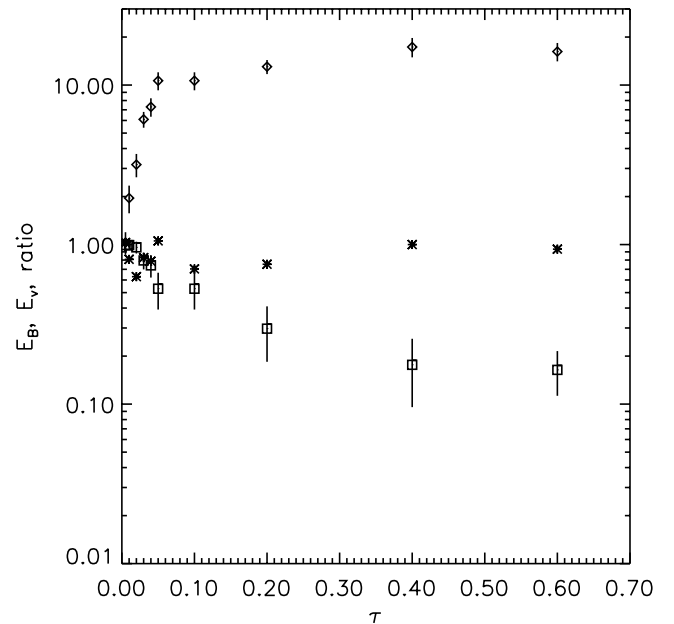

FIG. 9.—Magnetic (*circles*) and kinetic energy (*squares*) of saturated state in nonlinear solutions with varying velocity correlation time τ. The ratio $E_B/\rho\nu\gamma_B$, where γ_B is taken from Fig. 3 is shown by the asterisks. The ratio is very near 1, as predicted by eq. (26).
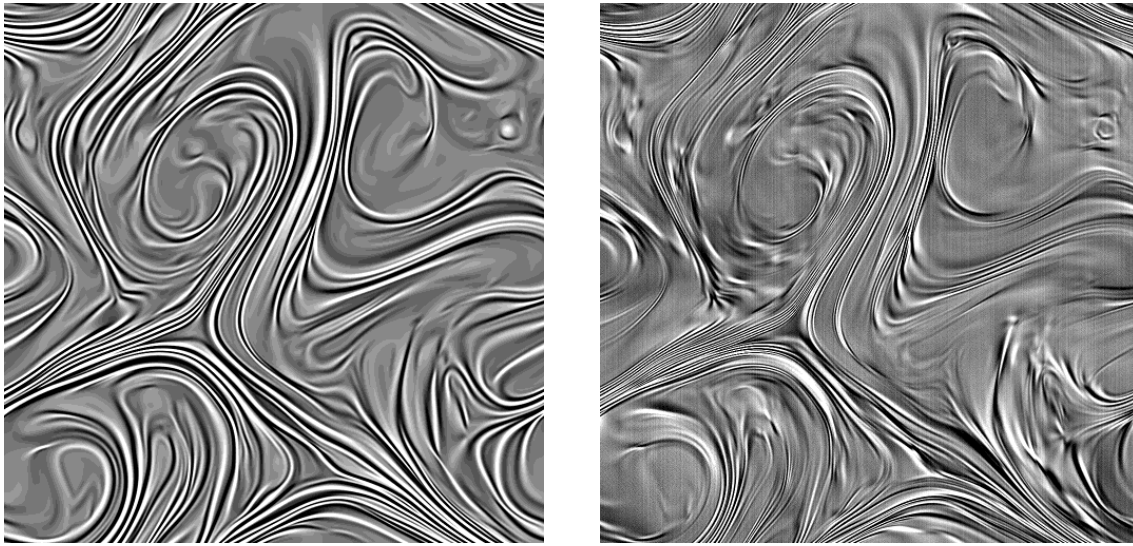
FIG. 10.—Visualization of the current (*left panel*) and ∇^2 vorticity (*right panel*) in a case with $\tau = 1$ and initial magnetic energy 0.1 during the saturated phase at $t = 5$. The small-scale component of the velocity (here accentuated by the ∇^2 operator) is primarily a flow along the local magnetic field lines. The large-scale velocity (not shown) is qualitatively the same as it would be in a kinematic solution, but with reduced amplitude.

netic and kinetic energy as a function of τ and $E_B / v \rho_0 \gamma_B$, where $\gamma_B(\tau)$ is the numerically measured kinematic growth rate shown in Figure 3. The predicted value of the saturated magnetic energy agrees quite well with the analysis.

In our analysis above, we have assumed that the shearing due to small-scale flows is negligible compared to large-scale flows. Because the geometry of the magnetic field is such that $|\boldsymbol{B} \cdot \nabla v| \ll |(\hat{z} \times \boldsymbol{B}) \cdot \nabla v|$ [i.e., $l_\perp \gg l_\parallel$, where $l_\perp(l_\parallel)$ is the local perpendicular (parallel) scale and we expect $l_\parallel \sim l_D$], then $\nabla \cdot v = 0$ implies $v_\parallel = v \cdot \hat{b} \sim v_\perp l_\parallel / l_\perp \gg v_\perp$. Thus, the small-scale flows are largely along the field lines. We can calculate the behavior of the small-scale flows from the curl of equation (2) for the chosen scalings, giving

$$\langle |v_\parallel(k)|^2 \rangle = \frac{\langle |\boldsymbol{B} \cdot \nabla B(k)|^2 \rangle}{\rho^2 v^2 k^4}. \tag{27}$$

A picture of the small-scale flows is given in Figure 10, which shows the current along with the Laplacian of the vorticity to emphasize the small velocity scales. The similarity of the geometry of the flows and field is evident.

Figure 11 shows the magnetic and kinetic energy spectra, at $t = 37$ for a case with $\tau = 1$ and initial magnetic energy 0.2. The spectra reach a quasi–steady state after saturation with the magnetic energy peaked at a scale intermediate between the largest scale and the resistive scale. Other solutions have similar spectra except for the location of this peak. The velocity spectrum shown is typical of all cases: a steep power law extending from the viscous to the resistive scale. This spectrum is remarkable for the absence of any feature near the peak in the magnetic spectrum. A fit of the spectrum in this range gives $E_v(k) \propto k^{-4.5}$. For comparison with equation (27), the spectrum of $|\boldsymbol{B} \cdot \nabla B(k)|^2 / k^4$ is also shown. The velocity spectrum is somewhat less steep than the prediction, but the agreement is fairly good.

Let us now consider the resistive evolution of the mean l_B in saturation. With no resistance, the averages of the system remain constant in the saturated state (i.e., $\langle B^2 \rangle$ and l_B are constant). However, with a small resistivity, the saturated state evolves so that l_B shrinks while $\langle B^2 \rangle$ is kept roughly constant, as seen in Figures 8 and 2. Resistivity weakens the field roughly at the rate η / l_B^2, and the velocity can, for $\langle B^2 \rangle < B_{\text{sat}}^2$, amplify $\langle B^2 \rangle$ at a rate γ_B. Thus, for $\gamma_B > \eta / l_B^2$,
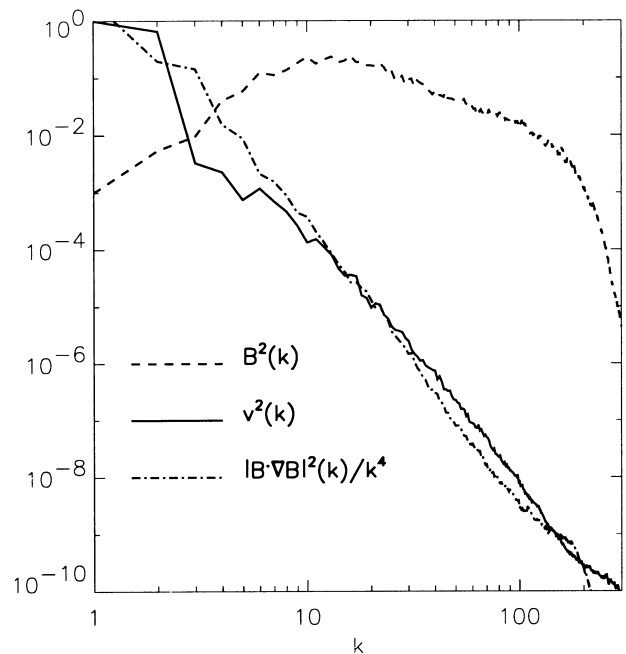

FIG. 11.—Spectra of magnetic energy (*dashed line*) and kinetic energy (*solid line*) in a nonlinear saturated state. The magnetic spectrum is peaked at the saturation scale. The velocity has a steep $k^{-4.5}$ power-law spectrum across all ranges. Also shown (*dot-dashed line*) is $|\boldsymbol{B} \cdot \nabla B(k)|^2 / k^4$ for comparison with eq. (27).
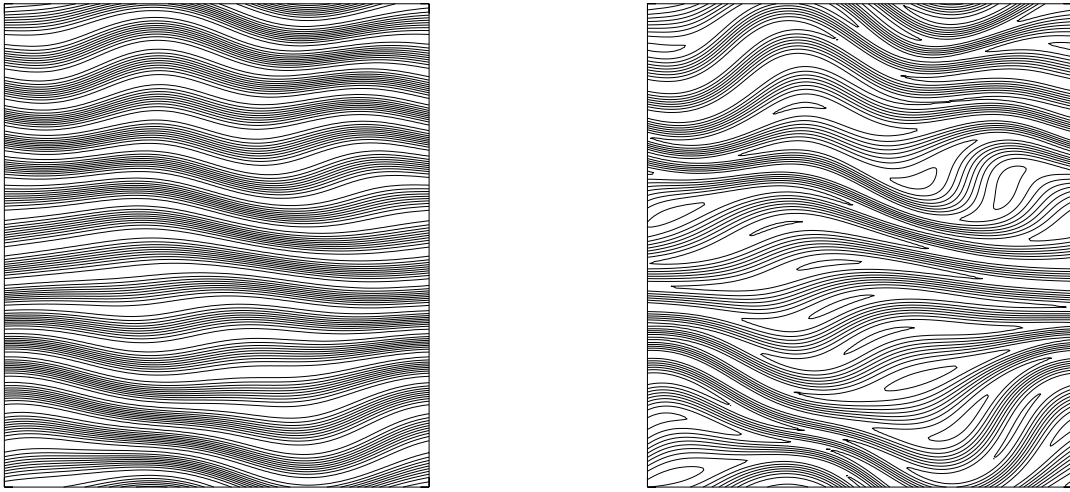
Fig. 12.—Idealized solution with strongly striped magnetic field. The driving velocity is stationary in time and the initial magnetic energy = 50. To the left are magnetic field lines at $t = 0.1$, soon after saturation. The magnetic field lines are distorted, and the velocity is only parallel to the local magnetic field. To the right is the solution at $t = 0.41$. The distortion of the field lines is greater after resistive weakening of the field lines. In addition, reconnection is forming magnetic loops. These loops can move in the fluid without resisting the flow with the tension in the field lines.

the magnetic field remains roughly constant with $\langle B^2 \rangle \sim B_{\mathrm{sat}}^2$. From equation (1) we obtain

$$\frac{d\langle A^2 \rangle}{dt} = -\eta \langle B^2 \rangle . \tag{28}$$

For $\langle B^2 \rangle =$ constant, and $\bar{k}$ defined in equation (3), we find

$$\bar{k}^2 \sim \frac{1}{1/k_{\mathrm{sat}}^2 - \eta t} , \tag{29}$$

with $k_{\mathrm{sat}}^2 = B_{\mathrm{sat}}^2/\langle A^2(0) \rangle \sim B_{\mathrm{sat}}^2/(B_I l_D)^2$ the average wavenumber at the start of saturation. We note that the evolution of $\bar{k}^2$ speeds up with time since the resistive *rate* $\eta \bar{k}^2$ increases in time. Thus, we estimate the duration of the saturated phase as the time required for $\bar{k}$ to approach l_R^{-1},

$$T_{\mathrm{sat}} = \frac{1}{\eta k_{\mathrm{sat}}^2} [1 - (l_R k_{\mathrm{sat}})^2] \sim \frac{B_I^2 l_D^2}{\eta B_{\mathrm{sat}}^2} . \tag{30}$$

The mechanism for increasing $\bar{k}$ can again be easily illustrated in an idealized solution with an initial "striped" magnetic field. Figure 12 shows magnetic field lines from a solution with initially large energy and a striped magnetic field. At saturation, the field lines are distorted and the flow is entirely along the magnetic field lines. This is a quasi–steady state in which the only evolution is resistive. As resistivity weakens the field lines, the flow winds them further, maintaining the same level of magnetic energy but decreasing the scale. At the same time, another effect of resistivity is to allow reconnection of magnetic field lines, which occurs on the timescale l_B^2/η, the same timescale on which the scale of the magnetic field evolves. The tension in these magnetic loops does not oppose the large-scale flow; the loops are simply moved around in the fluid. But the tension in the loops does oppose distortion of the loops. This prevents the field lines inside the loops from further stretching and thus being amplified back to saturation levels. It also prevents the loops from being distorted to small scales where they can be destroyed by resistivity.

5. NONLINEAR AND KINEMATIC DECAY PHASES

In two dimensions, the magnetic potential and the magnetic field must eventually go to 0 (Zeldovich 1957) as is evident from equation (28). Thus, at some point the field starts to decay. The decay happens in two distinct phases: the slower nonlinear decay phase followed by the kinematic decay phase. Figure 13 shows the full time history of several nonlinear solutions [with different initial field strength
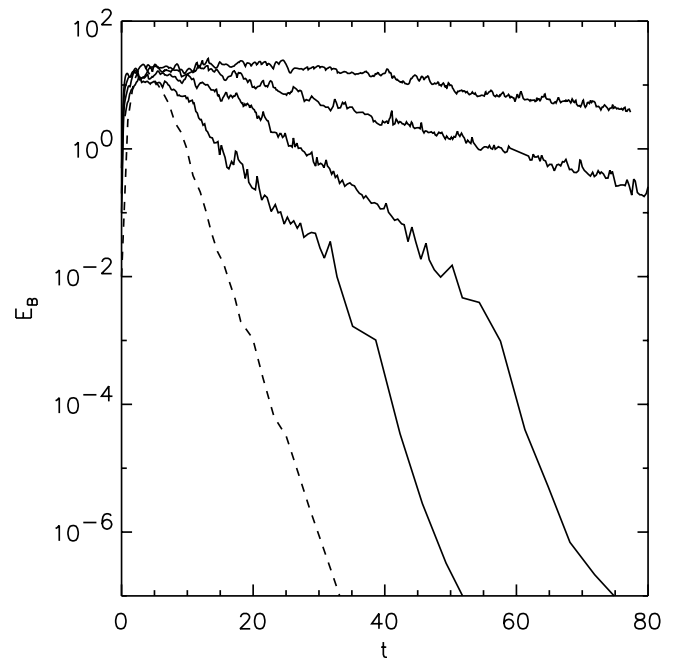

Fig. 13.—Energy vs. time for kinematic (*dashed line*) and nonlinear (*solid lines*) cases with $\tau = 1$. The nonlinear cases differ in the magnitude of the initial magnetic energy. In the earlier decay phase, the magnetic field decay is inhibited by nonlinear forces, but they all decay at the kinematic rate during the final phase.
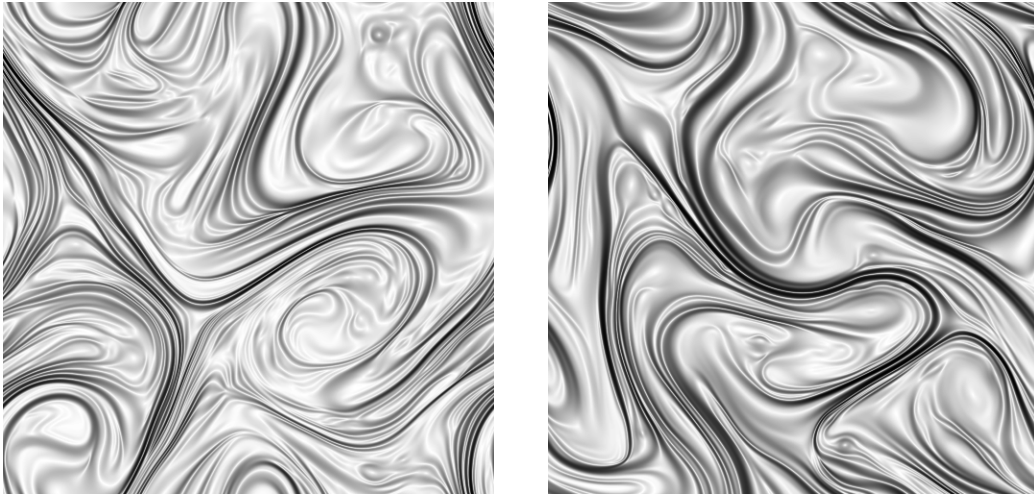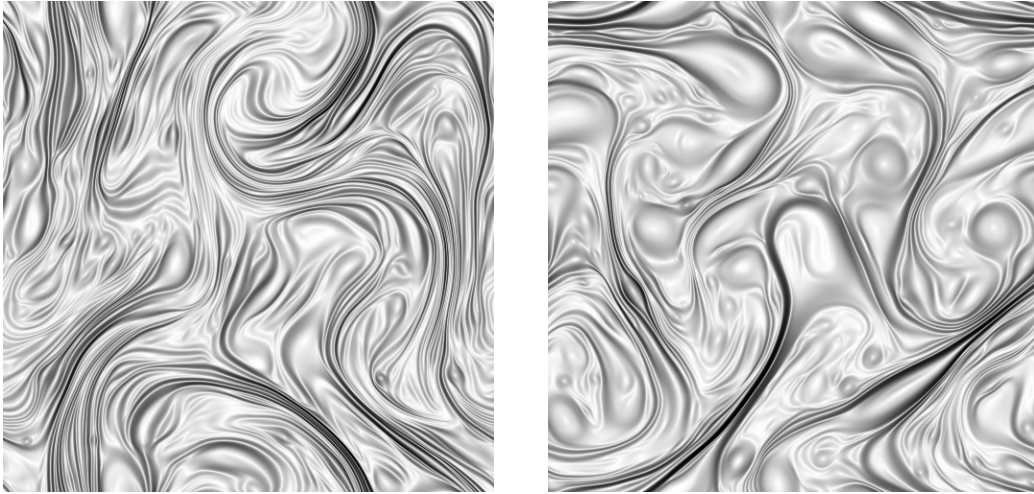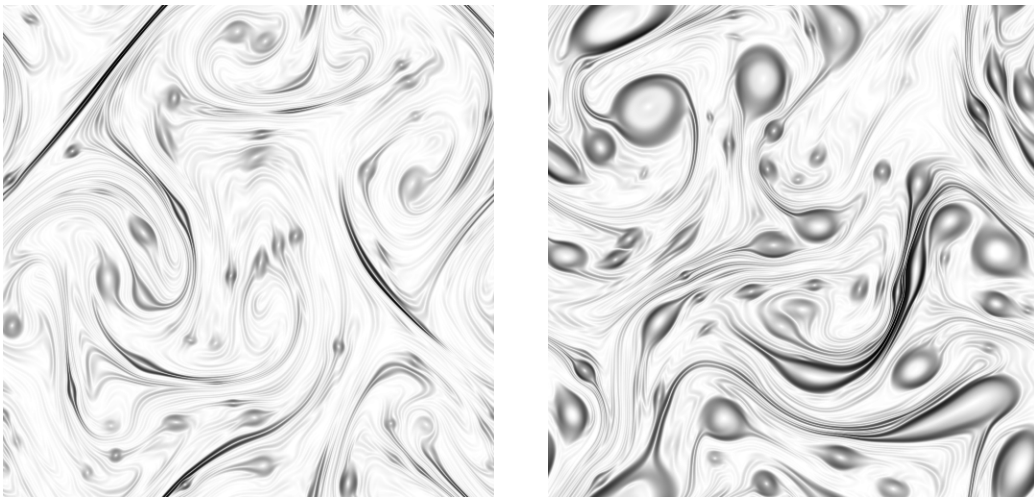
FIG. 14a

FIG. 14b

FIG. 14c

FIG. 14.—Visualizations of the magnetic field strength during saturation and nonlinear decay. Dark areas indicate larger values of $|\boldsymbol{B}|$. On the left is a solution with $E_B(0) = 0.1$ (Fig. 13, *third curve*). The solution on the right has $E_B(0) = 0.5$. In both cases, $\tau = 1$. (*a*) The fields early in the saturation phase ($t = 5$ and 11, respectively). The flux is dominated by sheets, and the sheets are thicker in the case with larger $E_B(0)$. (*b*) The fields near the end of the saturated phase ($t = 10$ and 30). Here, loops are beginning to emerge among the sheets, with larger loops coming from the case with thicker sheets. (*c*) The fields during the nonlinear decay phase ($t = 21$ and 50). The flux is dominated by loop structures which are decaying resistively while being advected by the flow. The solution with larger loop structures decays more slowly.

$E_B(0)$] along with one kinematic solution. For $E_B(0) = 0.05$, saturation ends at $t \approx 7$ and kinematic decay begins at $t \approx 30$, and for $E_B(0) = 0.1$ saturation ends at $t \approx 12$ and kinematic decay begins at $t \approx 50$. The kinematic decay rate is essentially the same for all solutions. However, the nonlinear decay rate is dependent on $E_B(0)$: the larger $E_B(0)$, the longer the saturation phase and the slower the nonlinear decay.

During the saturation phase the magnetic field has two coexisting structures: long folded structures, or current sheets (these were modeled as stripes in the previous section), and small-scale loops formed by resistive reconnection within the sheets. Loops of field tend to resist deformation during decay by trying to become circular, while sheets are stretched and therefore narrowed, hastening decay. Figure 14 shows visualizations of the magnetic field amplitude $|\boldsymbol{B}(\boldsymbol{x})|$ for two solutions with $E_B(0) = 0.1$ and 0.5 at three times: in the middle of the saturation phase, near the end of the saturation phase, and in the middle of the nonlinear decay phase. In Figure 14a most of the field amplitude is contained in sheets, with the sheet width larger in the case with larger $E_B(0)$.

As described in the previous section, the sheets continue to become stretched during saturation until $l_B = l_R$, when the stretching cannot compete with the resistive decay and the sheet field decays roughly at the rate γ as in equation (15). During saturation, resistive reconnection converts some fraction of the sheet field into loop structures. This process can be seen in Figure 12. It appears that this reconnection process is slower than the well-known "tearing mode" instability (Furth, Killeen, & Rosenbluth 1963) because viscosity damps the narrow flow structures necessary for accelerated reconnection. Instead, the reconnected flux grows linearly at a rate proportional to η. When a loop forms, its width perpendicular to $\boldsymbol{B}$, $l_\perp^{\text{loop}}$, must clearly satisfy $l_\perp^{\text{loop}} \lesssim l_B$ and its length along the field, $l_\parallel^{\text{loop}}$, may have values in the range $l_B < l_\parallel^{\text{loop}} \lesssim l_D$. In the direction along the sheets, the loop has field strength $B_\parallel \sim B_{\text{sat}}$, and in the direction perpendicular to the sheets, the strength is $B_\perp \sim B_\parallel \, l_\perp^{\text{loop}}/l_\parallel^{\text{loop}}$. Magnetic tension forces in the loop,

$$\boldsymbol{B} \cdot \nabla \boldsymbol{B} \sim \frac{B_\parallel^2}{l_\parallel^{\text{loop}}} \sim \frac{B_\parallel \, B_\perp}{l_\perp^{\text{loop}}}, \qquad (31)$$

act to turn the loop into a circle, whereas magnetic tension forces from the sheets outside the loop,

$$\boldsymbol{B} \cdot \nabla \boldsymbol{B} \sim \frac{B_{\text{sat}}^2}{l_\parallel^{\text{loop}}}, \qquad (32)$$

tend to squash the loop and keep $B_\parallel \sim B_{\text{sat}}$. If a loop became a circle, its radius would be $(l_\perp^{\text{loop}} l_\parallel^{\text{loop}})^{1/2}$ by conservation of volume and its field would be $B_{\text{circle}} \sim B_{\text{sat}}(l_\perp^{\text{sat}}/l_\parallel^{\text{sat}})^{1/2}$ by conservation of flux. The magnetic tension in such circular field lines is $(B_{\text{sat}}^2/l_\parallel^{\text{loop}})(l_\perp^{\text{loop}}/l_\parallel^{\text{loop}})^{1/2}$—too small to resist squashing by the tension in the sheets [which for the circle would be $(B_{\text{sat}}^2/l_\parallel^{\text{loop}})(l_\parallel^{\text{loop}}/l_\perp^{\text{loop}})^{1/2}$]. However, when a loop moves into a region where the sheets are weak, then the loop's magnetic tension dominates and the loop becomes more circular, as shown in Figure 15. During the
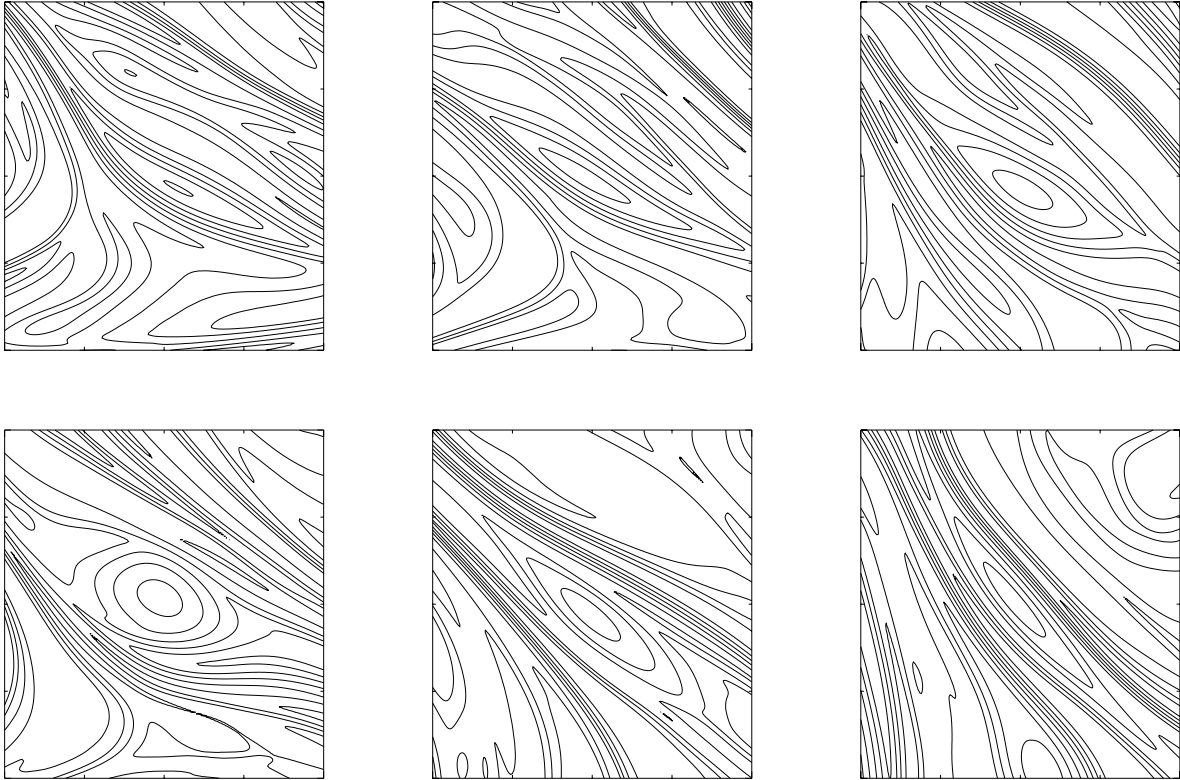

FIG. 15.—Detail of solution in Fig. 1, showing contour lines of A at $t = 3$–6. The squashed loop structure in the center becomes circularized when the sheets surrounding it weaken as the structure moves through a region with weak shear. The loop becomes squashed again when the sheets restrengthen. When the sheets finally are stretched to the resistive scale and disappear (after $t \approx 10$), the loop maintains its circular shape and gradually loses amplitude during the nonlinear decay phase.

saturation phase while the sheets maintain $B_\parallel \sim B_{\rm sat}$, this circularization is reversible when a loop moves back into a region with strong sheets.

Resistivity weakens the field in the sheets and in the loops. Because the loops are slightly fatter than the sheets, they decay more slowly. This difference is magnified by stretching, which continues to thin the sheets. The loops are also thin—so as to balance the tension forces of equations (31) and (32) and keep $B_\parallel = B_{\rm sat}$. However, since resistive decay is slower in the loops the thinning is also slower. Clearly, the sheets thin to $l_B = l_R$ first and the sheets are then rapidly destroyed, leaving the loops. This is the situation in Figure 14b, where loops are beginning to emerge from among the sheets. The loops are larger in the second solution, having been formed from thicker sheets.

When the sheets are destroyed, the tension in the loops, which are now considerably fatter than the sheets, is able to bring them to a circular shape (which is a stationary nonlinear solution of the MHD equations with $\eta = 0$ and $v = 0$). In Figure 14c, the field is dominated by loop structures. After becoming circles of radius $r = (l_\parallel^{\rm loop} l_\perp^{\rm loop})^{1/2}$, the loops will resist deformation by the sheared flow as long as the field in the loop ($B_{\rm loop}$) satisfies

$$B_{\rm loop}^2 > \frac{\rho v v_D}{l_D}\left(\frac{r}{l_D}\right)^2 = B_{\rm sat}^2\left(\frac{r}{l_D}\right)^2 . \qquad (33)$$

At the beginning of the nonlinear decay phase, all the loops satisfy this criterion. However, resistive decay will weaken the field in the loops so that

$$B_{\rm loop}^2(t) \simeq B_{\rm loop}^2(0) \exp\left(-\frac{\eta t}{r^2}\right)$$

$$\simeq B_{\rm sat}^2\left(\frac{l_B}{l_\parallel}\right)\exp\left(-\frac{\eta t}{l_B l_\parallel}\right), \qquad (34)$$

where we have taken $l_\perp = l_B$. Clearly, smaller loops ($l_\parallel$ smaller) decay faster. Loops will decay until they are too weak to resist the straining—for a given $l_\parallel$ this happens at a time $t = t_c$, where

$$\frac{\eta t_c}{2 l_D l_B} \simeq -\left(\frac{l_\parallel}{l_D}\right)\ln\left(\frac{l_\parallel}{l_D}\right). \qquad (35)$$

At the beginning of the nonlinear decay phase, there will be a distribution of loop sizes with $l_B < l_\parallel < l_D$ [or $l_B < r < (l_B l_D)^{1/2}$]. We are not able to predict this distribution. Once a loop has weakened enough to be strained, it will be rapidly destroyed by the combination of straining and resistive decay. The first loops to be destroyed are both the largest ones with $l_\parallel \sim l_D$ and the smallest with $l_\parallel \sim l_B$. Thus, as the nonlinear decay progresses, fewer and fewer loops persist. The longest surviving loop will have $l_\parallel \sim l_D/e$, a relatively large loop. This has some similarities to the increasing dominance of the largest coherent circular structure in two-dimensional neutral turbulence (McWilliams 1984) and two-dimensional $P_M \sim 1$ MHD turbulence (Kinney, McWilliams, & Tajima 1995 and references therein). When the last loop dies, the kinematic decay phase begins. During this final phase, the geometry of the magnetic field is once again that of narrow sheets at the resistive scale, and the overall magnetic energy decays exponentially as in a kinematic solution.

6. DISCUSSION

The calculations we have made here shed light on the processes necessary for generating a large-scale magnetic field in a high-P_M plasma such as the warm interstellar medium. The calculations here are two dimensional, and three-dimensional calculations will be reported later. The important results from two dimensions are the following.

The amplification of a weak seed magnetic field will initially occur at scales much smaller than the viscous dissipation scale. The scale of the magnetic field shrinks as the field strength grows, so that $B l_B \sim B_I l_D$. In two dimensions, this scale arrives at the resistive scale before Lorentz forces become dynamically important if the initial field is weak enough ($B_I^2 < \rho v_D^2 l_R^2/l_D^2$), or else it saturates at a larger scale if the initial field is stronger. If the magnetic energy saturates, the magnetic energy at saturation is independent of the initial energy, $B_{\rm sat}^2 \sim \rho v_D^2$, but the saturation scale increases with increasing B_I, $l_{\rm sat} \sim B_I l_D/B_{\rm sat}$. (In three dimensions, the field strength is able to continue to grow after the scale reaches the resistive scale, so the field can become nonlinear regardless of its initial strength.)

During the saturation phase, the field strength remains constant ($B \sim B_{\rm sat}$). However, the scale of the field, l_B, does decrease. This is due to a combination of resistivity, which weakens B, and stretching, which amplifies B back up to $B_{\rm sat}$ while decreasing l_B. The tension in the field lines counteracts the forced stirring of the fluid, resulting in a reduced kinetic energy at the stirring scale. In a solution that includes a turbulent inertial range, this would correspond to a decrease in kinetic energy at the dissipation scale. How the saturated evolution is changed by the presence of an inertial range is as yet not clear.

During the saturation phase, sheets of current reconnect to form loops embedded in sheets. The loops are flattened by the magnetic pressure in the sheets but remain slightly thicker than the sheets because magnetic tension pulls the ends of the loops together. During saturation, the sheets continue to be stretched to smaller thicknesses, but the shear in the driving flow across a loop is not strong enough to drive them to smaller scales. When the sheets reach the scale where resistive decay is faster than stretching, they dissipate away, leaving behind loops which quickly circularize because of magnetic tension. In the first decay phase, the nonlinear decay phase, the magnetic energy is contained mostly in the loops, which decay resistively at a rate depending on their size. The size of the loops depends on the thickness of the sheets out of which they were formed, which depends on the initial magnetic energy. Eventually the loops become too weak to resist deformation by the flow and are strained to the resistive scale, after which the decay is as in the kinematic scenario.

A complete discussion of the evolution of field in the galaxy must wait until a forthcoming paper on three-dimensional behavior. However, the behaviors of MHD turbulence in two dimensions and three dimensions are generally more similar than in neutral turbulence, and there are many aspects of our two-dimensional results that we expect to see in three dimensions, for example, exponential growth during the kinematic phase and saturation at a wavenumber independent of resistivity (for η sufficiently small). The behavior after saturation in three dimensions is expected to be quite different, since there is no requirement that the field decay to 0 at infinite time.

The field referred to in this paper as the saturated field, $B_{\rm sat}$, is roughly the field required to be in equipartition with the eddies at the viscous scale of the turbulence. This is unlikely to be affected by the dimensionality of the domain and can be estimated $B_{\rm sat}^2 \sim \rho v_D^2 \sim \rho v_0^2\, R^{-1/2} \approx 0.2\text{–}0.4\ \mu{\rm G}$ for the warm ISM. The observed field has a strong large-scale component and is roughly in equilibrium with the turbulent kinetic energy ($B^2 \sim \rho v_0^2$) at a strength 2–4 μG. Because the known mechanisms for producing seed fields in the galaxy give initial field strength $10^{-22}\ {\rm G} \lesssim B_0 \lesssim 10^{-3}$ μG, it is a virtual certainty that the seed magnetic field in the galaxy is weak enough to become highly tangled during turbulent amplification, yet strong enough that magnetic forces will become important before the tangles reach the resistive scale. Thus, it is critical to study the nonlinear evolution of the tangled state, with $l_R \gg l_B \ll l_D$ and $B^2 \sim B_{\rm sat}^2$. Our study has revealed characteristics of this evolution, such as the halting of forward cascade of magnetic energy and the structure of the velocity and magnetic fields at this scale range, that have direct bearing on the understanding of the origin of galactic fields.

APPENDIX

MODEL EQUATIONS AND NUMERICAL METHOD

Our equations are the usual incompressible MHD equations. The magnetic field obeys an induction equation

$$\partial_t \boldsymbol{B} = \boldsymbol{\nabla} \times (\boldsymbol{v} \times \boldsymbol{B}) + \eta \nabla^2 \boldsymbol{B}\,, \tag{A1}$$

while the velocity field obeys a momentum equation

$$\partial_t \boldsymbol{v} + \boldsymbol{v} \cdot \boldsymbol{\nabla} \boldsymbol{v} = \nu \nabla^2 \boldsymbol{v} + (\boldsymbol{\nabla} \times \boldsymbol{B}) \times \boldsymbol{B} - \boldsymbol{\nabla} p + \boldsymbol{F}(t) \tag{A2}$$

with p chosen to ensure $\boldsymbol{\nabla} \cdot \boldsymbol{v} = 0$. Although these equations are familiar, they are not usually solved in the high–Prandtl number regime of large viscosity and small resistivity. In this Appendix, we describe the numerical methods we have developed for this parameter regime in order to calculate solutions more efficiently.

The large Prandtl number implies that the magnetic field will vary on scales much smaller than the velocity field, which is dominated by the large-scale forcing. The highly tangled magnetic field may be transported over many grid points without significant distortion, so a scheme that avoids the usual CFL constraint on the time step $v\Delta t < \Delta x$ is desirable. Our method is related to the COSMIC scheme for scalar advection (Leonard, Lock, & MacVean 1996). Referring to Figure 16, let $B_x(i, j)$ be the magnetic flux through the line connecting the points (i, j) and $(i, j - 1)$, and let $r_0(i, j)$ denote the point obtained by
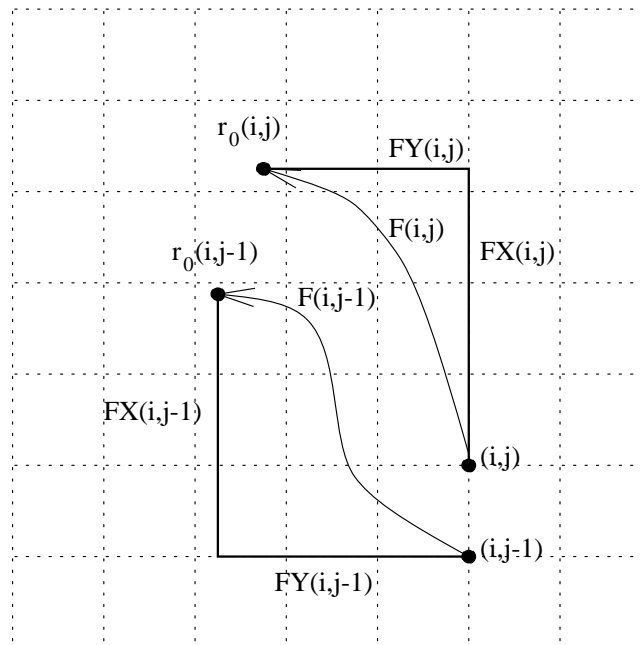

FIG. 16.—Numerical scheme for vector advection equation with arbitrary time step

integrating back along a velocity streamline for time Δt, starting from the grid point (i, j). The "frozen field" condition of ideal MHD states that the magnetic flux through any surface moving with the fluid is constant in time. Thus,

$$B_x(i, j, t + \Delta t) = \mathbf{B}(t) \cdot [\mathbf{r}_0(i, j) - \mathbf{r}_0(i, j - 1)] . \tag{A3}$$

Denote the magnetic flux at time t through the streamline connecting (i, j) and $\mathbf{r}_0(i, j)$ by $F(i, j)$. Because $\mathbf{B}$ is divergence free,

$$B_x(i, j, t + \Delta t) - B_x(i, j, t) = F(i, j) - F(i, j - 1) , \tag{A4}$$

where F can be similarly decomposed

$$F(i, j) = FX(i, j) + FY(i, j) ,$$
$$F(i, j - 1) = FX(i, j - 1) + FY(i, j - 1) . \tag{A5}$$

Here, FX and FY are fluxes through lines parallel to the computational grid, which are computed by first calculating the integrated flux of $\mathbf{B}$ through lines that lie on the computational grid,

$$\Phi_x(i, j) = \sum_{j'=0}^{j} B_x(i, j') ,$$
$$\Phi_y(i, j) = \sum_{i'=0}^{i} B_y(i', j) , \tag{A6}$$

and then interpolating these integrals to the appropriate points,

$$FX(i, j) = \Phi_x[i, r_{0y}(i, j)] - \Phi_x(i, j) ,$$
$$FY(i, j) = \Phi_y[r_0(i, j)] - \Phi_y[i, r_{0y}(i, j)] . \tag{A7}$$

Because Φ is related to the vector potential A, this integration of the fluxes is equivalent to replacing the vector potential at a point (i, j) by its value at the upstream point $r_0(i, j)$.

To complete the method, we must specify an interpolation function to determine $\Phi(x)$ from the grid-based values. This interpolation function determines the spatial accuracy of the method. We use a cubic interpolation in each of the two dimensions. The temporal accuracy is determined by the accuracy in integrating a streamline to obtain r_0, for which we use an iterative predictor-corrector scheme. To allow for the possible change in direction of a streamline between t and $t + \Delta t$, we allow an optional interpolation of the velocity field forward in time as the streamline is traced.

The dissipation of the magnetic field due to resistivity is calculated implicitly,

$$(1 - \eta \, \Delta t \nabla^2)\mathbf{B}(t + \Delta t) = \mathbf{B}(t) , \tag{A8}$$

where the inversion of the $(1 - \eta \, \Delta t \nabla^2)$ operator can be carried out by a spectral or iterative method. In order to reduce the effects of finite resistivity as much as possible, we often use a hyperresistive dissipation operator $(1 + \eta_4 \, \Delta t \nabla^4)$. A value of η_4 is calibrated to a value of η if they result in the same value of $\bar{k}$ during a kinematic dynamical solution (i.e., they have the same resistive scale). Generally, the qualitative behavior of our solutions does not change with the use of hyperresistivity, and the same scalings arguments based on resistive scale l_R apply for hyperresistivity if the scale is calculated as $l_R^4 \sim l_D \eta/v$. Figure 17 compares the evolution of E_B for Newtonian and hyperresistive solutions. Both solutions have the same essential behavior of growth, saturation at $t \approx 1$, and decay beginning at $t \approx 20$, although the energy for most of the saturated phase is smaller for the hyperresistive solution. Visualizations of the fields have the same appearance at all times. Because the hyperresistive solution has a resistive cutoff nearer the grid scale, it can be calculated on a grid $\frac{1}{4}$ the size of the Newtonian solution. Equivalently, we can calculate solutions with much smaller resistivity (hence, higher Prandtl number) at the same cost by using a hyperresistive operator.

To solve the momentum equation, we must specify a sensible forcing function $\mathbf{F}(t)$. We choose an $\mathbf{F}$ which gives the appropriate velocity spectrum in the viscous dissipation range (Chen et al. 1993),

$$\mathbf{F}(k) = \mathbf{k} \times \hat{\mathbf{r}}(\mathbf{k}, t) k^{\alpha_1} e^{\alpha_2 \, k} e^{i\phi(\mathbf{k}, t)} , \tag{A9}$$

where $\alpha_1 \approx 1.9$ and $\alpha_2 \approx 1.5$ are constants, $\hat{\mathbf{r}}$ is a randomly oriented unit vector, and ϕ is a random phase. The correlation time τ is controlled by choosing independent random values for $\hat{\mathbf{r}}$ and ϕ at each $\mathbf{k}$ at time $t = n\tau$ for integer n and interpolating in time to find the phases at intermediate times.

The momentum equation can be advanced by a standard time-centered predictor-corrector scheme, but resolving the viscous decay timescale introduces a severe constraint on the time step. This can be alleviated by implementing an implicit scheme, in which the velocity is given by

$$(1 - v \, \Delta t \nabla^2)\mathbf{v}(t + \Delta t) = \mathbf{v}(t) + \Delta t \mathbf{v} \cdot \nabla \mathbf{v} + (\nabla \times \mathbf{B}) \times \mathbf{B} - \nabla p + \mathbf{F} . \tag{A10}$$

We choose a time step based on the advective timescale, $\Delta t \nabla v \sim 1$. Because the scales are deep within the viscous range, $v \nabla^2 v \gg v \nabla v$, so that $v \, \Delta t \nabla^2 v \gg v$, and the momentum equation is well approximated by the simple diagnostic relation

$$v \nabla^2 \mathbf{v} = -(\nabla \times \mathbf{B}) \times \mathbf{B} + \nabla p - \mathbf{F} ,$$
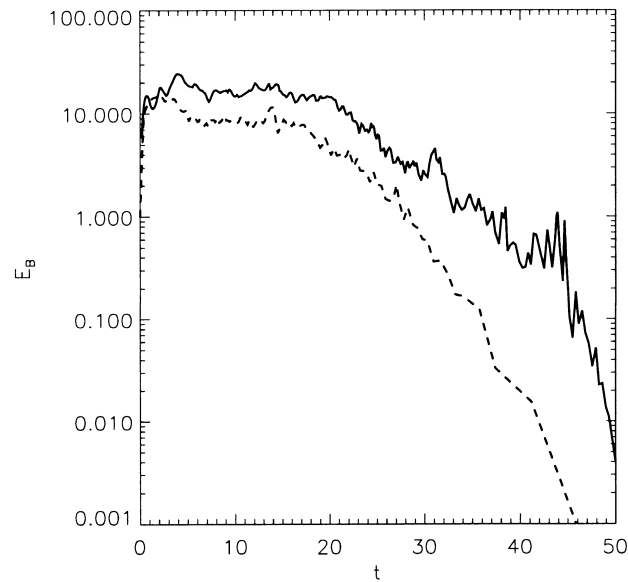$$\nabla \cdot \mathbf{v} = 0 , \tag{A11}$$

FIG. 17.—Comparison of E_B vs. time for Newtonian resistivity (*solid line*) and hyperresistivity (*dashed line*). The solutions pass through the same phases at approximately the same times with similar values of the energy and decay rates.

which is a balance between Lorentz and viscous forces. Because F is chosen to give the empirical spectrum of dissipation-range turbulence, this balance is valid independent of the amplitude of B. However, this approximation is only valid deep within the dissipation range and breaks down as one approaches the viscous scale. Because the scale of B remains below the largest available scale of the computational domain for all solutions reported here, this is a valid method for computing v.

REFERENCES

Balsara, D., & Pouquet, A. 1999, Phys. Plasmas, 6, 89
Batchelor, G. K. 1950, Proc. R. Soc. London A, 201, 405
Braginskii, S. I. 1965, in Reviews of Plasma Physics, Vol. 1, ed. M. A. Leontovich (New York: Consultants Bureau), 205
Brandenburg, A., & Donner, K. J. 1997, MNRAS, 288, L29
Cattaneo, F., & Hughes, D. 1996, Phys. Rev. E, 54, R4532
Chandran, B. 1997, ApJ, 485, 148
Chen, S., Doolen, G., Herring, J. R., Kraichnan, R. H., Orszag, S., & She, Z. S. 1993, Phys. Rev. Lett., 70, 3051
Childress, S., & Gilbert, A. 1995, Stretch, Twist, Fold: The Fast Dynamo (Berlin: Springer)
Cowling, T. G. 1957, J. Mech. Appl. Math., 10, 129
Field, G., Blackman, E., & Chou, H. 1999, ApJ, 513, 638
Furth, H. P., Killeen, J., & Rosenbluth, M. N. 1963, Phys. Fluids, 6, 459
Goldreich, P., & Sridhar, S. 1995, ApJ, 438, 763
Gruzinov, A. V., Cowley, S. C., & Sudan, R. 1996, Phys. Rev. Lett., 77, 4342
Kazantsev, A. P. 1968, Soviet Phys. JETP, 26, 1031
Kinney, R. M., & McWilliams, J. C. 1998, Phys. Rev. E, 57, 7111
Kinney, R., McWilliams, J. C., & Tajima, T. 1995, Phys. Plasmas, 2, 3623
Kraichnan, R. H. 1965, Phys. Fluids, 8, 1385

Kraichnan, R. H. 1976, J. Fluid Mech., 75, 657
Kulsrud, R. M., & Anderson, S. W. 1992, ApJ, 396, 606
Kulsrud, R. M., Cen, R., Ostriker, J., & Ryu, D. 1997, ApJ, 480, 481
Larson, R. B. 1979, MNRAS, 186, 479
Leonard, B. P., Lock, A. P., & MacVean, M. K. 1996, Mon. Weather Rev., 124, 2588
McWilliams, J. C. 1984, J. Fluid Mech., 146, 21
Meneguzzi, M., Frisch, U., & Pouquet, A. 1981, Phys. Rev. Lett., 47, 1060
Moffatt, H. K. 1978, Magnetic Field Generation in Electrically Conducting Fluids (Cambridge: Cambridge Univ. Press)
Oughton, S. 1996, J. Plasma Phys., 56, 641
Parker, E. N. 1979, Cosmical Magnetic Fields (Oxford: Clarendon)
Pouquet, A., Frisch, U., & Léorat, J. 1976, J. Fluid Mech., 77, 321
Quataert, E. 1998, ApJ, 500, 978
Ruzmaikin, A. A., Shukurov, A. M., & Sokoloff, D. D. 1988, Magnetic Fields of Galaxies (Dordrecht: Kluwer)
Spangler, S. R., & Cordes, J. M. 1998, ApJ, 505, 766
Zeldovich, Y. B. 1957, Sov. Phys. JETP, 4, 460
Zweibel, E. G., & Heiles, C. 1997, Nature, 385, 131